Flame soot absorption coefficient and temperature reconstruction through line-of-sight attenuation and light field imaging

Tianxiang Ling[1], Guoqing Chen[2], Md. Moinul Hossain[3], Qi Qi[1,3], Biao Zhang[1], Chuanlong Xu[1*]

(1. National Engineering Research Center of Power Generation Control and Safety, School of Energy and Environment, Southeast University, Nanjing 210096, China)

(2. State Key Laboratory of Low-Carbon Smart Coal-fired Power Generation and Ultral-clean Emission, China Energy Science and Technology Research Institute Co., Ltd, Nanjing 210096, China)

(3. School of Engineering, University of Kent, Canterbury, Kent, CT2 7NT, UK)

(Email: chuanlongxu@seu.edu.cn)

Abstract: The accuracy and efficiency of 3-D flame temperature field reconstruction using the light field imaging technique heavily depend on soot radiation characteristics. In this study, we employ the line-of-sight attenuation method to reconstruct the soot absorption coefficient distribution in a pure absorbing flame. Utilizing these soot absorption coefficients, the radiative transfer equation is effectively transformed within the framework of the light field imaging technique into a linear inverse problem and also outlines the flame boundary. This proposed strategy reduces the unwanted detection rays significantly, thus eliminating the extensive computational processing. Consequently, the proposed approach substantially enhances the accuracy and efficiency of flame temperature reconstruction. Numerical simulations were carried out on a bimodal asymmetric flame to validate the noise tolerance capabilities, investigate the effects of varying voxel numbers on flame division and carry out a comparative study. Experimental studies were also conducted to reconstruct flame temperature and soot absorption coefficient distributions under different combustion operating conditions. Thermocouple measurements were performed and compared with the reconstructed temperatures. Outcomes achieved from both numerical simulations and experimental studies demonstrate the feasibility, accuracy and robustness of the proposed method.

Keywords: Line-of-sight attenuation; Light field imaging; Soot absorption coefficient; Flame temperature; 3-D reconstruction

1. Introduction

Combustion, which is pervasive across various industries such as power generation, aerospace, metallurgy and chemical industry, encompasses a range of applications such as coal-fired boilers, internal combustion engines, gas turbines and other combustion applications. Precise measurement of three-dimensional (3-D) flame temperature during the combustion process plays a crucial role in understanding combustion mechanisms comprehensively and optimizing the combustor configurations. Traditionally, the temperature of hydrocarbon flames is determined by characterizing the soot temperature, because soot serves as the primary participating medium within the flame [1]. The soot particles released from the combustion process due to incomplete combustion and the soot particles have been identified as harmful to human health and environment [2, 3]. The formation of soot also exerts a substantial influence on the flame temperature distribution, primarily through their significant contribution to radiative heat transfer [4]. Moreover, the flame temperature governs the rates of physical and chemical reactions, thereby controlling the formation and oxidation of soot. Hence, it is of utmost importance to measure both soot and flame temperature accurately while striving to understand their inherent coupling relationship [5, 6].

Various methods have been developed for measuring soot and flame temperature measurements, among them emission-based optical diagnostic techniques have gained significant attention due to their non-invasive nature, fast response time and ease of system setup [7]. Efforts have been made to determine the flame temperature and soot radiative properties (or soot volume fraction) simultaneously using optical emission tomography [8-10]. However, these techniques exclusively rely on a single camera and are restricted to axisymmetric flames study. High-precision reconstruction of 3-D asymmetric flames necessitates the use of multiple cameras and associated optics. For instance, Huang et al. [11] developed a stereoscopic image system, which comprises four precisely arranged mirrors to obtain flame projections. Hossain et al. [12] utilized eight optical imaging fibers and two RGB Charge-coupled Device (CCD) cameras to acquire the sooty flame images from eight directions. Ni et al. [13] proposed a multispectral imaging system that consists of four symmetrical CCD cameras and liquid crystal tunable filters (LCTF). In these studies, the 3-D soot temperature and volume fraction distributions of asymmetric flames were successfully retrieved. However, the practical application of these studies has been hindered by the synchronization and calibration complexities associated with multi-camera systems. The light field imaging (LFI) technique has gained widespread attention due to its ability to record both spatial and angular information in a single exposure. The LFI facilitated by a light field camera (LFC) has successfully been applied to 3-D imaging of particle tracking velocimetry, fuel sprays and depth estimation measurements [14-16]. When applied to the 3-D flame temperature reconstruction, the LFI technique partitions the flame into interconnected 3-D voxels. By employing a reconstruction algorithm, the temperatures of these voxels can be determined by solving radiative transfer equations (RTE) [17]. However, the soot radiative properties are often unknown and coupled with the flame temperature in practical flames, rendering the RTE a nonlinear equation system. Consequently, solving the RTE for reconstructing the flame temperature sets a nonlinear inverse problem. To address this problem, two primary strategies have been proposed:

(1) develop a reconstruction algorithm to retrieve the flame temperature and soot radiative properties simultaneously. To achieve that, a series of gradient-based [18-20] or intelligent optimization-based [21, 22] hybrid algorithms have been proposed. For instance, Li et al. [19] proposed a hybrid algorithm called Levenberg-Marquardt with boundary constraint and non-negative least squares (LMBC-NNLS) to reconstruct the flame temperature and

absorption coefficient simultaneously. Niu et al. [21] introduced a hybrid algorithm called least-square QR decomposition-stochastic particle swarm optimization (LSQR-SPSO) for the simultaneous reconstruction of flame temperature distribution and radiative properties. However, the gradient-based algorithms require solving the Jacobian matrix, while the intelligent optimization-based algorithms involve extensive random searches. These factors significantly reduce the computational efficiency and limit the spatial resolution of the reconstructed results.

(2) convert nonlinear inverse problems into linear inverse problems by incorporating a priori information regarding soot radiative properties. For example, Sun et al. [17] considered the absorption coefficient of 0.8 m^{-1} and utilized the LSQR algorithm to reconstruct the 3-D flame temperature fields. Qi et al. [23, 24] set the absorption coefficient to 10 m^{-1} and reconstructed the flame temperature based on the non-negative least squares (NNLS) algorithm. However, the morphology and chemical composition of soot undergoes substantial changes as soot particles evolve within the flame [25]. Initially, nascent soot particles exhibit a "liquid-like" transparent nature [26] and demonstrate limited absorption of visible light beyond wavelengths of 600 nm [27]. As the particles mature, they transform into aggregated solid carbonized spheres with well-defined boundaries [28], acquiring broad-band light absorption capabilities [29]. The distinct properties of nascent and mature soot particles increase notable disparities in the radiative properties of soot particles and self-absorption within optically thick flames. These differences can introduce uncertainties when inferring temperatures. To investigate the impact of these variations, Yuan et al. [30] conducted simulations to investigate the impact of varying soot absorption coefficient values of 5, 10, 25, and 50 m^{-1} on temperature reconstruction. The study shows that when the absorption coefficients increase, the longitudinal section images of the flame show a diminishing intensity. When the absorption is very intense, the irradiance of flame longitudinal sections is so small that cannot be discerned. Li et al. [31] also studied the effect of nonuniform soot radiative properties on the effectiveness of flame temperature reconstruction. These studies demonstrated that soot radiative properties play a significant role in determining the flame temperature accurately.

It is therefore crucial to obtain precise information on soot radiative properties before conducting LFI-based flame temperature reconstruction. The diode lasers can be integrated with laser absorption and flame emission measurements for an accurate measurement of soot radiative properties. Studies [32-34] have successfully utilized the absorption/emission technique to determine the one-dimensional (1-D) or two-dimensional (2-D) fields of soot temperature and radiative parameters in axisymmetric flame. However, the 3-D fields of non-axisymmetric flame have rarely been studied.

In this work, a hybrid method is proposed for reconstructing 3-D soot absorption coefficient and flame temperature distributions. The proposed method combines the LFI technique with the line-of-sight attenuation (LOSA) method to improve the efficiency and accuracy of flame temperature reconstruction. It leverages the LOSA method to obtain the soot absorption coefficient distribution, which is subsequently utilized as prior information in the LFI technique. Additionally, the flame boundary is pre-identified using the soot absorption coefficient distribution, thereby improving the overall temperature reconstruction efficiency. Numerical simulations were conducted on a bimodal flame to assess the feasibility and practicality of the proposed method. This evaluation encompassed an examination of its noise tolerance capabilities, a comparative analysis against presently employed LF reconstruction methods, and an exploration of the impact of voxel count variations on flame division. Furthermore, experimental investigations were conducted to validate the proposed method under various flame distributions and combustion

operation conditions. Measurement principles and numerical and experimental studies are introduced and analyzed in detail.

2. Methodology

The overall strategy for reconstructing 3-D soot absorption coefficient and flame temperature distributions encompasses two main components. The LOSA method is employed to determine the soot absorption coefficient distribution first and the LFI technique is then used to obtain the temperature distribution. This proposed model integrates the principles of both LOSA and LFI to improve the accuracy and efficiency of the reconstructed soot absorption coefficient and temperature distributions. In this study, a bimodal flame is used as an illustrative example, A bimodal flame refers to a combustion process in which two distinct flame types or combustion modes coexist within the same system, as visually represented in Fig. 1. This choice is primarily driven by its direct relevance to practical scenarios commonly encountered in combustion systems. The subsequent paragraphs provide a comprehensive explanation of the LFI and LOSA principles, as well as the proposed hybrid reconstruction model.

2.1. Light field imaging

The LFC mainly consists of a main lens, a microlens array (MLA) and a photosensor, which can capture the spatial and angular information of the flame radiation by a single exposure [35]. The schematic of the flame radiation sampling through the LFC is depicted in Fig. 1.

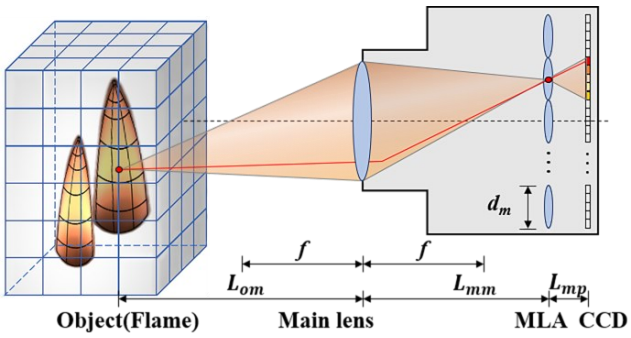

Fig. 1. The schematic of the flame radiation sampling through the LFC.

Where L_{om} is the distance between the flame centerline and the main lens, L_{mm} is the distance between the main lens and MLA, L_{mp} is the distance between the MLA and the CCD, f is the focal length of the main lens, d_m the diameter of each microlens.

Each radiation ray emitted from the flame can be sampled successively by the main lens and the MLA. According to the pinhole camera model [36], the sampling ray can be traced in reverse, starting from the pixel on the CCD sensor and extending towards the corresponding point in the flame. The direction information of the ray is then traced through the main lens plane and the MLA plane. The detailed tracing model can be found in [37].

The intensity detected by a pixel is regarded as the intensity of the corresponding ray, which can be calculated using the RTE [38].

$$\frac{dI_\lambda(s,\mathbf{\Omega})}{ds} = -K_\lambda^{(a)}(s)I_\lambda(s,\mathbf{\Omega}) + K_\lambda^{(a)}(s)I_{b\lambda}(s) \tag{1}$$

where $I_\lambda(s,\mathbf{\Omega})$ is the radiation intensity at position s and direction $\mathbf{\Omega}$ at wavelength λ, $I_{b\lambda}$ is the blackbody

radiative intensity at wavelength λ, $K_\lambda^{(a)}$ is the absorption coefficient.

The radiation intensity of the flame $I_\lambda(s,\mathbf{\Omega})$ along the detection path $(s,\mathbf{\Omega})$ is then obtained by solving Eq. (1) through the discretized solution as follows,

$$I_\lambda(s,\mathbf{\Omega}) = I_{b\lambda}^{nn}\left[1-\exp\left(-r_{nn}K_{\lambda nn}^{(a)}(s)\right)\right] + \sum_{i=1}^{nn-1}\left[\exp\left(-\sum_{j=i+1}^{nn} r_j\,K_{\lambda j}^{(a)}(s)\right)-\exp\left(-\sum_{j=i}^{nn} r_j\,K_{\lambda j}^{(a)}(s)\right)\right]I_{b\lambda}^{i} \tag{2}$$

where nn is the total number of voxels that the flame radiation passes through, and each voxel is kept at a uniform temperature. i and j are the ith and jth voxel along the flame detection path $(s,\mathbf{\Omega})$, respectively. r denotes the length of the detection path in the ith voxel.

The out-going radiative intensity of the whole detection field received by the LFC can therefore be obtained by integrating Eq. (2) in different detection directions, which can be written as follows:

$$\boldsymbol{I_\lambda} = \boldsymbol{A_\lambda}\cdot\boldsymbol{I_{b\lambda}} \tag{3}$$

where $\boldsymbol{I_\lambda}$ is the flame radiative intensity vector; $\boldsymbol{I_{b\lambda}}$ is the blackbody radiative intensity vector; $\boldsymbol{A_\lambda}$ is the coefficient matrix. Typically, Eq. (3) is a nonlinear equation since the soot absorption coefficient is unknown in practical flames. The dependence of the blackbody radiative intensity $\boldsymbol{I_{b\lambda}}$ and the temperature T is expressed by

$$I_{b\lambda}(s) = \frac{c_1\lambda^{-5}}{\pi[e^{c_2/\lambda T(s)}-1]} \tag{4}$$

where c_1 and c_2 are the first and second radiation constants, respectively.

2.2. Line-of-sight attenuation

LOSA is a well-established optical method for path-averaged measurement of the soot extinction coefficient in an aerosol. In this method, the transmissivity of an aerosol-containing medium is measured for a linear path and defined as

$$\tau_\lambda = \frac{I_\lambda}{I_{\lambda,0}} = \exp\left(-\int_{-\infty}^{\infty} K_\lambda^{(e)}\,ds\right) \tag{5}$$

where τ is the transmissivity of the path at wavelength λ. $I_{\lambda,0}$ and I_λ are the light intensity before and after passing through the flame, respectively. $K_\lambda^{(e)}$ is the local extinction coefficient.

It is noticed that the scattering contribution to extinction is negligible in the upper band of the visible spectrum [39]. Thus, the local absorption coefficient $K_\lambda^{(a)}$ is equivalent to $K_\lambda^{(e)}$ according to Rayleigh-Debye-Gans-Polydisperse-Fractal-Aggregate (RDG-PFA) theory [40].

As noted above, a single transmissivity measurement can only provide a measure of the path-averaged soot absorption coefficient. Thus, to obtain the 2-D absorption coefficient distributions, measurements along multiple chords through the flame are crucial. The schematic of the 2D-LOSA principle is depicted in Fig. 2.

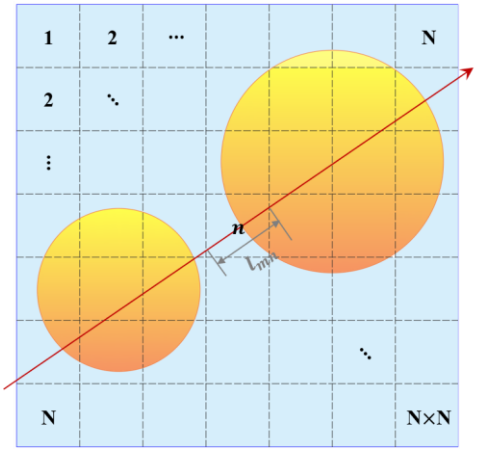

Fig. 2. The schematic of the 2-D-LOSA method.

It can be seen that the soot absorption coefficient is inhomogeneous in the cross-section, normal to the bulk flow direction of the flame. The computational domain is divided into discrete grids (N×N), with the absorption coefficient considered to be consistent within each grid. Calculating the distance l of light m passing through each grid, Eq. (5) can be rewritten as

$$\ln\left(I_\lambda / I_{\lambda,0}\right) = l_{m1}K_{\lambda 1}^{(a)} + l_{m2}K_{\lambda 2}^{(a)} + \cdots + l_{mn}K_{\lambda n}^{(a)} \tag{6}$$

where n denotes the number of grids passed by light.

To integrate each light in multiple directions, Eq. (6) can be expressed in matrix form as

$$\boldsymbol{I} = \boldsymbol{L} \cdot \boldsymbol{K} \tag{7}$$

where $\boldsymbol{I}$ is the calculated transmissivity vector and $\boldsymbol{L}$ is the distance coefficient matrix.

Eq. (7) is a typical linear equation system. The absorption coefficient matrix $\boldsymbol{K}$ can be solved by a reconstruction algorithm, such as the NNLS algorithm [41]. Based on the reconstructed absorption coefficient distribution, the grids containing flame information (with orange in Fig. 2) can be identified. The flame boundary can further be recognized by excluding the grids that contain no flame information.

2.3. Proposed hybrid reconstruction model

To reconstruct the 3-D soot absorption coefficient and flame temperature distributions precisely and efficiently, a hybrid reconstruction model is proposed. The proposed method incorporates the soot absorption coefficient distribution, obtained through the LOSA method, as prior information within the framework of the LFI technique. By employing this strategy, the nonlinearity and ill-posed nature of the inverse problem to reconstruct the flame temperature is mitigated, as it effectively converts it into a linear inverse problem. Consequently, this method significantly improves the accuracy of reconstructing the flame temperature field. Also, the effective detection rays for temperature reconstruction are reduced, which can improve the reconstruction efficiency. The overall process of the reconstruction model is summarized as follows.

Step 1. Dividing the flame into discrete layers along the bulk flow direction. For each cross-section, divide the computational domain into discrete grids as illustrated in Section 2.2. Calculating the transmissivity vector $\boldsymbol{I}$ and distance coefficient matrix $\boldsymbol{L}$, and solving Eq. (7) for obtaining the absorption coefficient matrix $\boldsymbol{K}$ by NNLS algorithm. This step involves acquiring the distribution of the 2-D absorption coefficient within the discrete cross-

section of the flame.

Step 2. Based on the absorption coefficient distribution obtained in Step 1, the 2-D flame-containing grids (filled in orange color in Fig. 2) are identified by applying a threshold. The grids above the threshold are considered flame-containing grids. The threshold value is set at zero in accordance with physical prior distributions, as the soot absorption coefficient for grids without flame containment is determined to be zero. This step is repeated layer-by-layer to obtain the flame-containing voxels for the 3-D absorption coefficient field.

Step 3. Dividing the flame into discrete voxels, maintaining consistency with Step 1. For the flame image recorded by the LFC, performing ray tracing on each pixel, as illustrated in Section 2.1. Deleting the invalid ray if the ray does not pass through any flame-containing voxels, which are pre-recognized in Step 2.

Step 4. To transform the flame image into an intensity distribution, calibrating the radiation intensity of the LFC. Subsequently, calculating the flame radiative intensity vector $\boldsymbol{I_\lambda}$ using the gray levels of the CCD pixels for the effective rays filtered after Step 3.

Step 5. Calculating the coefficient matrix $\boldsymbol{A_\lambda}$ with the absorption coefficient resolved in Steps 1-2. Solving Eq. (3) for obtaining the blackbody radiative intensity vectors $\boldsymbol{I_{b\lambda}}$ by the NNLS algorithm and achieving the 3-D temperature field by solving Eq. (4).

The flowchart of the reconstruction method is summarized and depicted in Fig. 3.

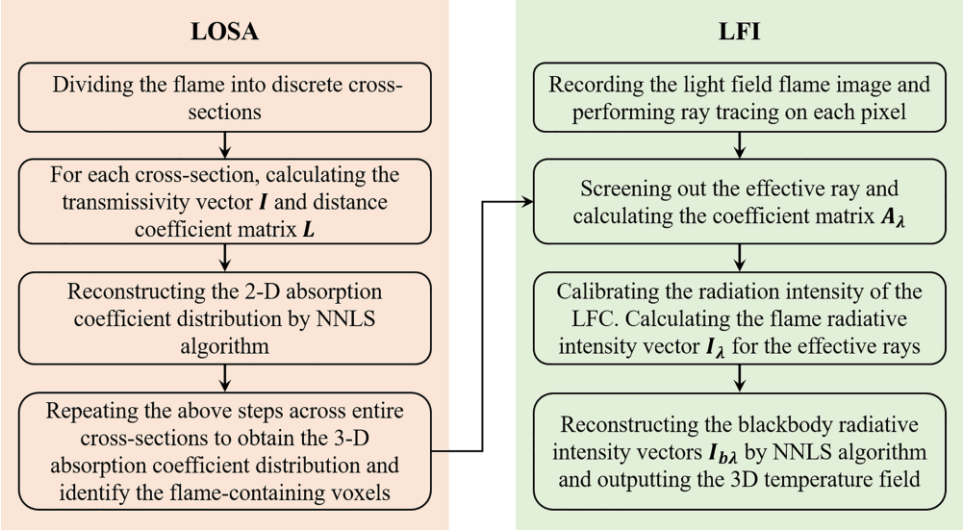

Fig. 3. The flowchart of the reconstruction model.

3. Numerical Study

Numerical simulations were conducted to verify the feasibility and practicality of the proposed method. A bimodal asymmetric cylindrical ethylene flame is simulated and the NNLS algorithm is used to reconstruct the soot temperature and absorption coefficient. The radius (R) and height (Z) of the cylindrical flame was set to 6.6 mm and 25 mm, respectively. The flame is divided into axial (N_z)×radial (N_r)×circumferential(N_φ)= 6 × 8 × 10 voxels. The parameters of the LFC used in the simulation are shown in Table 1. The temperature and absorption coefficient distribution were generated through Eqs. (8)-(9) [21, 42], respectively. Within each voxel, the flame temperature and absorption coefficient are assumed to be uniform and are defined by the value at the center point. The distributions of flame temperature and absorption coefficient are illustrated in Fig. 4.

$$T(x,y,z)=\frac{2200}{3}\left(\begin{array}{c}\exp\left\{\begin{array}{c}-40[(750x+7.5)/9-1.1]^2\\-25[(750y+8.5)/9-0.8]^2\end{array}\right\}\\+0.8\exp\left\{\begin{array}{c}-25[(750x+7.5)/9-0.8]^2\\-35[(750y+8.5)/9-1.2]^2\end{array}\right\}\end{array}\right)+880\left(1-\frac{100z}{3}\right)+753[\mathrm{K}] \tag{8}$$

$$K(x,y,z)=\frac{50}{3}\left(\begin{array}{c}\exp\left\{\begin{array}{c}-40[(750x+7.5)/9-1.1]^2\\-25[(750y+8.5)/9-0.8]^2\end{array}\right\}\\+0.8\exp\left\{\begin{array}{c}-25[(750x+7.5)/9-0.8]^2\\-35[(750y+8.5)/9-1.2]^2\end{array}\right\}\end{array}\right)+20\left(1-\frac{100z}{3}\right)+5/3\,[\mathrm{m}^{-1}] \tag{9}$$

where x, y, z are the coordinates of the cylindrical flame, respectively.

Table 1. Parameters of the light field camera.

Symbol	Value	Description
L_{om}/mm	505	the distance between the flame centerline and the main lens
L_{mm}/mm	53.1	the distance between the main lens and MLA
L_{mp}/mm	480	the distance between the MLA and the photosensor
f/mm	50	the focal length of the main lens
$f_m/\mu m$	600	the focal length of the microlens
$d_p/\mu m$	8	the length of the pixel
$d_m/\mu m$	95	the diameter of each microlens
N_m	60	the number of microlenses
N_p	12	the number of pixels covered by each microlens
M	1.11	the magnification of the lens

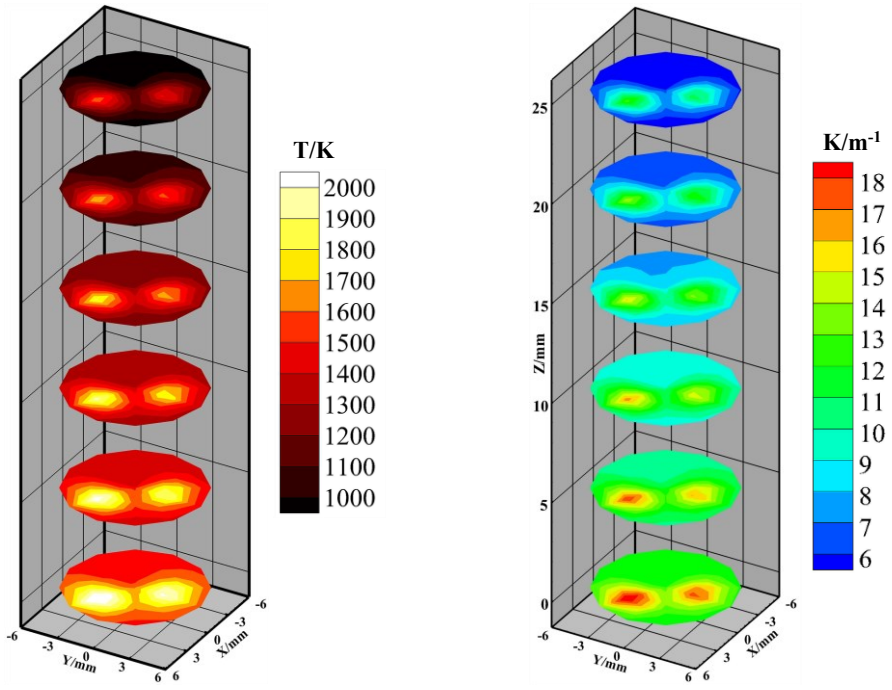

Fig. 4. The simulated flame temperature and absorption coefficient distributions.

The simulations were performed on a server with Intel Core i9-9900K CPU @ 3.60 GHz and 64.0 GB RAM. The simulation procedures were executed utilizing MATLAB R2019b.

The effects of noise levels and flame-dividing voxels on the reconstruction performance are investigated and discussed in Sections 3.1 to 3.3. To evaluate the reconstruction performance, the relative reconstruction errors of temperature ΔT_i and absorption coefficient ΔK_i in the ith voxel are calculated based on Eqs. (10)-(11). The mean reconstruction relative errors of temperature ΔT_{mean} and absorption coefficient ΔK_{mean} are also calculated according to Eqs. (12)-(13).

$$\Delta T_i = \frac{\left|T_{rec,i} - T_{ori,i}\right|}{T_{ori,i}} \tag{10}$$

$$\Delta K_i = \frac{\left|K_{rec,i} - K_{ori,i}\right|}{K_{ori,i}} \tag{11}$$

$$\Delta T_{mean} = \frac{1}{N}\sum_{i=1}^{N} \Delta T_i \tag{12}$$

$$\Delta K_{mean} = \frac{1}{N}\sum_{i=1}^{N} \Delta K_i \tag{13}$$

where subscripts rec,i and ori,i are the reconstructed and original values, respectively; N is the total number of voxels of the flame.

3.1. Effects of noise levels

To investigate the noise tolerance capability of the proposed method, different noise levels (γ) were considered. The noise levels are added randomly using Eq. (14):

$$I_{mea} = (1 + \sigma\xi) I_{exa} \tag{14}$$

where I_{mea} is the actual detected signal, I_{exa} is the exact signal without noise, ξ is a standard normal distribution random variable. The standard deviation (STD) is determined for the measured transmittance and reflectance σ for a γ at 99% confidence as

$$\sigma = \frac{I_{exa} \times \gamma}{2.576}. \tag{15}$$

The noises γ =1%, 3% and 5% are considered and their corresponding signal-to-noise ratios (*SNR*s) of 48 dB, 38 dB and 34 dB are defined by Eq. (16):

$$SNR = 10\log_{10}\left[\frac{\sum_{i=1}^{k}\left(I_{exa}^{i}\right)^2}{\sum_{i=1}^{k}\left(I_{mea}^{i} - I_{exa}^{i}\right)^2}\right] \tag{16}$$

where k is the grid number of the flame.

Two different sources of noise are investigated in the study. Firstly, for the absorption coefficient reconstruction, noise is introduced to the transmissivity vector $\boldsymbol{I}$ in Eq. (7). Secondly, for temperature reconstruction, noise is added to the flame radiative intensity vector $\boldsymbol{I_\lambda}$ in Eq. (3). The reconstruction results that have been derived in this study are based on the average of ten calculations. The impact of these noises on the overall reconstruction performance is systematically evaluated as outlined below.

(1) For the absorption coefficient reconstruction, the laser arrays are set from 0 mm to 25 mm with an axial

interval of 5 mm. The flame is divided into $N_r \times N_\varphi = 8 \times 10$ grids and the lasers are evenly spaced at 45° intervals in 8 directions for each cross-section of the flame. In each direction, the lasers are parallel with an interval of 0.1 mm, thus, a total of 1056 rays are obtained. The noises γ = 1%, 3% and 5% are added to I_λ in Eq. (5) for each cross-section. The reconstructed absorption coefficient distributions and relative errors under different noise levels are illustrated in Fig. 5. It shows that both the mean and maximum relative errors increase with the noise levels. The ΔK_{mean} is 1.64% for γ = 5%, which demonstrates an excellent noise tolerance capability for the absorption coefficient reconstruction. In all cases, the measured average time from the entire dataset for all runs ranged between 4.1 and 4.7 seconds, demonstrating the high efficiency of absorption coefficient reconstruction.

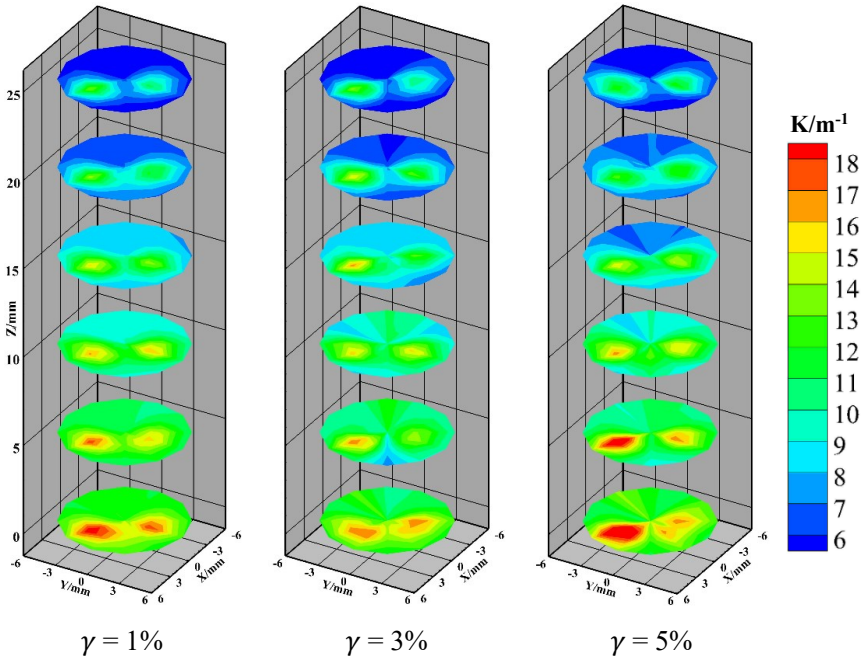

(a) Absorption coefficient distributions of flame cross-sections.

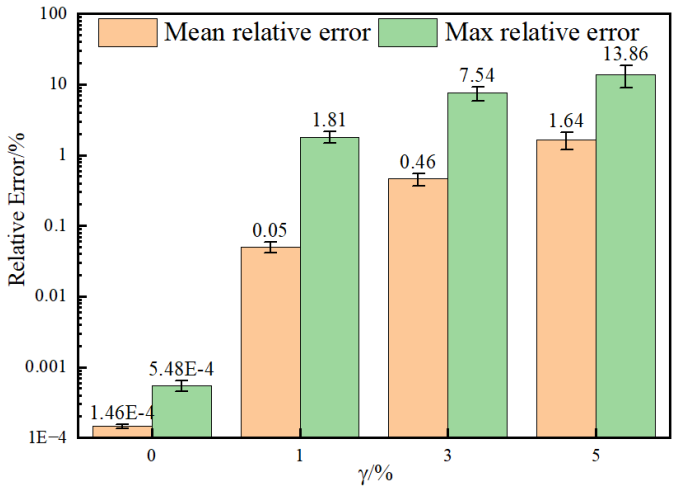

(b) Relative errors.

Fig. 5. Reconstructed flame absorption coefficient distributions and relative errors under different noise levels.

(2) For temperature reconstruction, the reconstructed absorption coefficient under the γ = 1% is considered as the prior information to retrieve the flame temperature. Only the area containing the flame information is used for

reconstruction. As a result, the voxels are reduced from 480 to 95 and correspondingly, the feature rays are reduced from 29209 to 18660. The noise levels γ = 1%, 3% and 5% are added to the flame radiative intensity. The reconstructed temperature distributions and relative errors under different noise levels are illustrated in Fig. 6. The mean and maximum relative errors increase slightly with the noise levels and the mean temperature reconstruction relative error is 1.01% even for γ = 5%, which demonstrates the superior noise tolerance capability for the temperature reconstruction. The reconstruction time at all noise levels is about 1s, demonstrating that the proposed method can reconstruct the flame temperature with high efficiency.

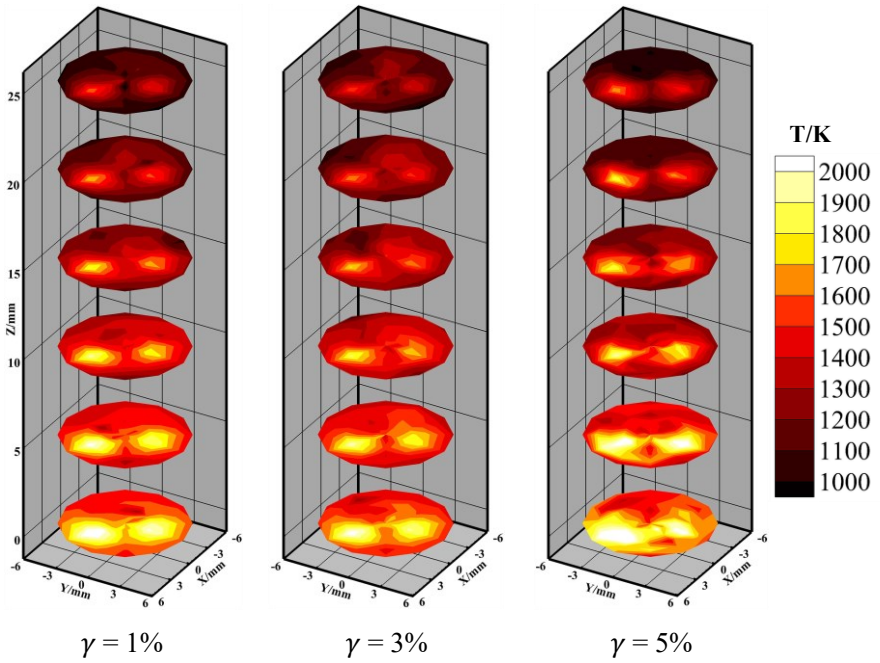

(a) Temperature distributions of flame cross-sections.

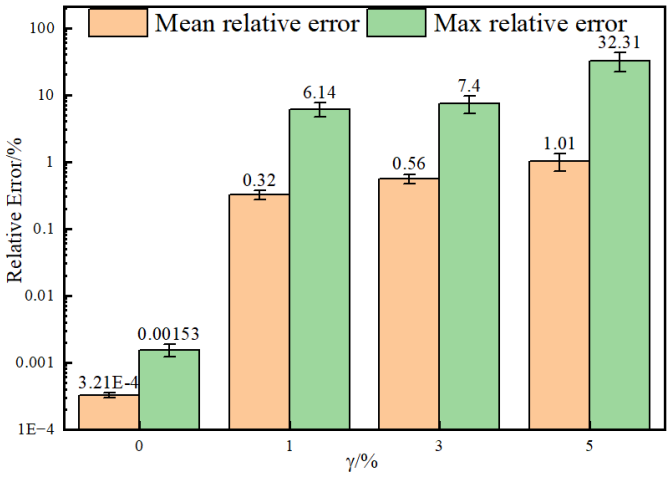

(b) Relative errors.

Fig. 6. Reconstructed flame temperature distributions and relative errors under different noise levels.

3.2. Comparative study

To verify the reconstruction performance of the proposed method, a comparative study is conducted with the

recent studies [19, 30]. This assessment includes the presentation of three distinct Cases, as outlined below.

Case 1: reconstructing the flame temperature by utilising the soot absorption coefficient of 10 m^{-1} [30].

Case 2: reconstructing the soot absorption coefficient and temperature simultaneously by the LMBC (Levenberg-Marquardt with Boundary Constraint)-NNLS algorithm [19].

Case 3: the proposed method without extracting the flame-containing voxels and filtering the effective ray.

The reconstructed temperature distributions under different Cases are illustrated in Fig. 7. The overview of the reconstruction performance under different Cases is presented in Table 2. Remarkably, the execution time reported in this study is to solve Eq. (3) for various reconstruction methods and the execution times are calculated under consistent conditions, such as temperature and absorption coefficient distributions, dividing voxels, and noise levels. Notably, these calculations were conducted using identical processing platforms, operating systems, configurations, and associated programming libraries.

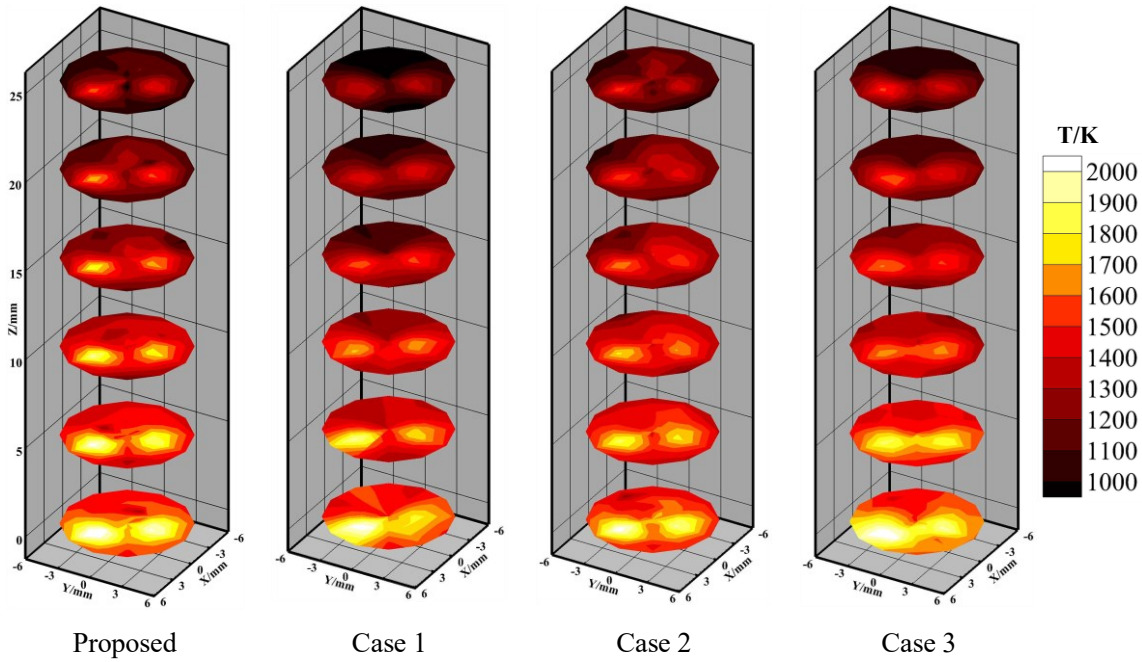

Fig. 7. Reconstructed flame temperature distributions under different Cases.

Table 2. The reconstruction error and time under different reconstruction methods.

Case	ΔT_{mean}/%	ΔT_{max}/%	ΔK_{mean}/%	ΔK_{max}/%	Reconstruction time/s
Proposed	0.32	6.14	0.05	1.81	5.68(1.23+4.45)
Case 1 [30]	6.78	32.16	/	/	169.34
Case 2 [19]	7.46	30.88	15.46	50.88	112790
Case 3	2.84	25.9	/	/	147.61

The results demonstrate that the proposed method yields minimum relative errors and reduced reconstruction times for both the absorption coefficient and temperature. Specifically, the total reconstruction time for the proposed method is about 5.68s, where 1.23s is for the flame temperature reconstruction and 4.45s is for the absorption

coefficient reconstruction. The relative error of temperature exhibited an impressive reduction of at least 88%, while the reconstruction time was reduced by a noteworthy minimum of 95%. In Case 1, the temperature reconstruction error increased due to the constant absorption coefficient, which effectively added noise to the coefficient matrix in Eq. (3). In Case 3, for reconstructing the temperature, the absorption coefficient utilized is closer to the true value as determined by Eq. (9), thus reducing the reconstruction error slightly compared to Case 1. However, in Case 3, the effective flame voxels (containing the flame information) and ray selection are not considered, leading to ill-conditioning and an increased dimension of the reconstruction matrix in Eq. (3). Consequently, this approach decreases the reconstruction accuracy and increases the computational cost compared to the proposed method. In Case 2, the reconstruction time is substantially higher compared to the other cases because the reconstruction algorithm is required to solve the Jacobian matrix, which inherently demands more computational time. Therefore, the results suggested that the proposed method can reconstruct the soot absorption coefficient and temperature accurately with a shorter reconstruction time.

3.3. Effects of flame dividing voxels

The size of the flame voxel has a significant impact on reconstruction accuracy. If the voxel size is too large, the detailed flame information may be lost, resulting in lower reconstruction accuracy. In contrast, if the voxel size is too small, the larger data is required to be processed and increases the computational cost. Six different flame-dividing voxels ($N_z \times N_r \times N_\varphi$) were considered to investigate the effect of the flame voxels on the temperature reconstruction performance. The noise level of γ = 1% is considered for the absorption coefficient and temperature reconstruction. The absorption coefficient distribution obtained in Section 3.2 is utilized in two distinct approaches to reconstruct the flame temperature: the proposed method and the original sampling. Notably, the proposed method incorporates the flame-containing voxels and an effective ray selection process, in contrast to the original sampling, which does not involve the extraction of flame-containing voxels. The reconstruction parameters and time achieved under different flame-dividing voxels are illustrated in Table 3.

Table 3. The number of voxels, feature rays and reconstruction time.

Case	Dividing voxel	Number of voxels and feature rays		Reconstruction time/s	
		Original sampling	**Proposed method**	Original sampling	**Proposed method**
1	3×4×5	60-29209	12-13626	0.7	0.05
2	4×6×8	192-29209	36-15522	14	0.11
3	6×8×10	480-29209	96-18660	148	1.23
4	8×10×12	960-29209	218-19833	945	8.94
5	10×12×15	1800-29209	329-20263	7789	23.48
6	12×15×20	3600-29209	710-21557	45226	422

A significant reduction in reconstruction time can be seen by the proposed method. For instance, for the $N_z \times N_r \times N_\varphi$ = 8×10×12, the number of voxels decreased from 960 to 218 and the feature rays reduced from 29209

to 19833. Consequently, the reconstruction time reduced significantly from about 945s to 8.94s. (i.e., efficiency increased by 99%). It is therefore evident that the reconstruction time increases significantly as the dividing voxel size increases. Whereas the number of voxels and feature rays required for the reconstruction increases with the dividing voxel size but not like the reconstruction time.

The performance of the flame temperature reconstruction is also investigated for the original sampling and the proposed method. The reconstruction error under different flame-dividing voxels are shown in Fig. 8. The proposed method reconstructs the flame temperature field accurately with a considerable reduction of maximum error of 24.76% and the mean relative error of 67.89% compared to the original sampling. Therefore, the proposed method simplifies the reconstruction process even for relatively larger flame-dividing voxels, thus improving the reconstruction accuracy and efficiency, effectively.

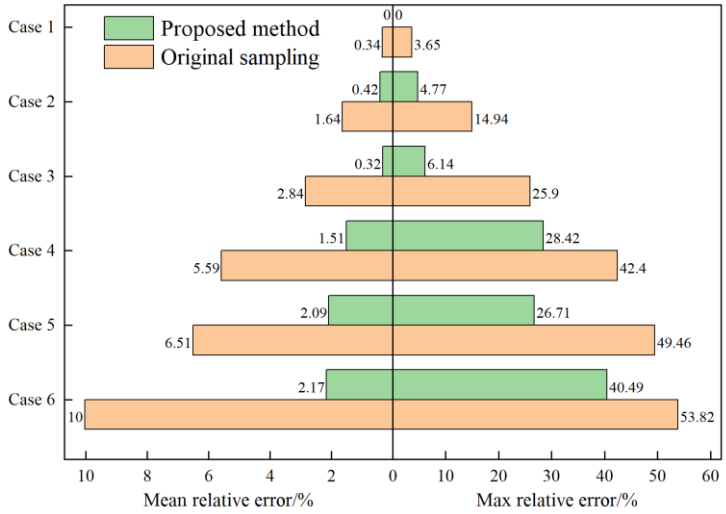

Fig. 8. Temperature reconstruction error under different flame-dividing voxels.

4. Experimental evaluation

Further to verify the proposed method, experiments were carried out to reconstruct the 3-D absorption coefficient and temperature distribution of ethylene (C_2H_4) diffusion flames. A monochrome LFC is used to capture the flame images under different operation conditions. The structure of the LFC is shown in Fig. 9(a). The focal length of the main lens is 50 mm. The size of the MLA is 100×100 μm, with a corresponding f-number of 4.2. The photosensor (i.e., JHUM 204B) has a resolution of 1920 (H)×1200 (V) with a pixel size of 5.86 μm. The detailed structure of the LFC can be found elsewhere in [23]. Bimodal laminar non-axisymmetric ethylene diffusion flames were generated through a co-flow burner at atmospheric pressure. A replaceable two-nozzle plate was positioned at the central point of the co-flow burner. The structure of the burner is shown in Fig. 9(b). It consists of two 8 mm inner diameter nozzles for fuel injection surrounded by a 50 mm inner diameter co-annular tube for co-flow air supply. The geometric structure of the burner plate can be found elsewhere in [43]. The burner is placed on a supporting plate that can be lifted and rotated. Two mass flow controllers (Sevenstar CS200A) were used to supply constant flow rates of ethylene fuel and air. Three different combustion operation conditions were considered and listed in Table 4. Example flame images of these three conditions are shown in Fig. 10. In addition, a Gülder laminar axisymmetric diffusion flame burner was also used to validate the feasibility of the proposed method [44]. In this burner, ethylene

fuel is supplied through a central nozzle. The outside and inner diameters of the nozzle are 12.7 mm and 10.9 mm, respectively. Air is supplied through a co-annular tube with an inner diameter of 100 mm. Detailed information regarding the Gülder burner can be found elsewhere in [45].

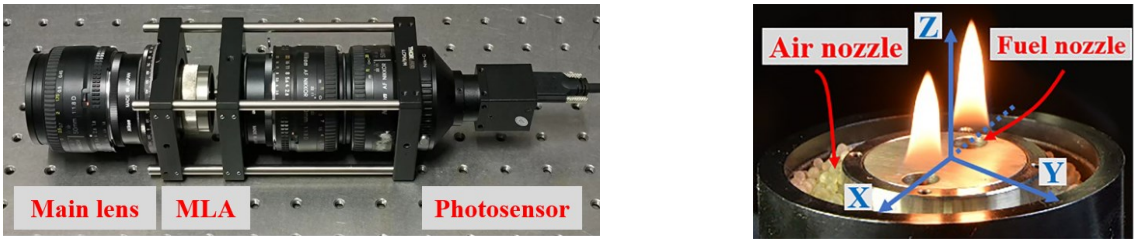

(a) Structure of LFC (b) Structure of the bimodal flame burner

Fig. 9. Main parts of the experimental setup.

Table 4. Experimental conditions of bimodal flame.

Condition	Ethylene (L/min)	Air (L/min)
1	0.10	3
2	0.12	3
3	0.15	3

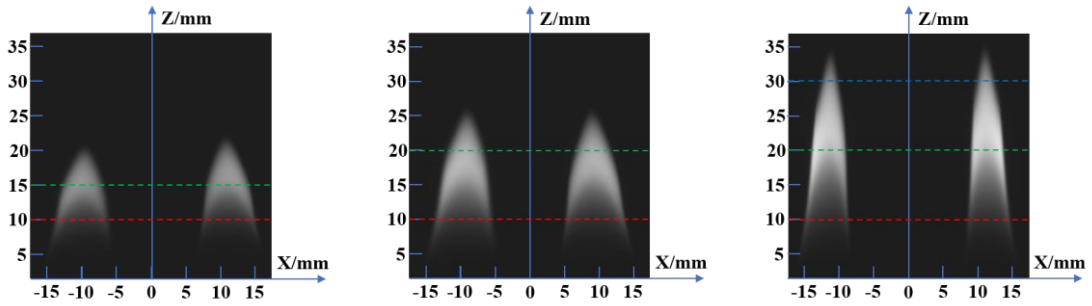

(a) Condition 1 (b) Condition 2 (c) Condition 3

Fig. 10. Example flame images captured under three operation conditions.

An experiment of LOSA measurement [46] was performed using the optical configuration as shown in Fig. 11 to obtain transmissivity flame images. The pulsed LED lamp (Thorlabs M660L4) is coupled to an integrating sphere (Thorlabs IS236A-4) to provide a uniform diffused light source. The diffuse light is then collimated into a beam by a collimating lens (AC508-300-AB-ML) and incident on the flame. The light beam passing through the flame is converged by two imaging lenses (AC508-400-AB-ML), the first lens focuses the light onto the aperture and the second lens re-collimates the light [45]. The re-collimated beam is then captured by the CCD sensor coupled with a Nikon 50 mm lens. The transmissivity measurement is achieved consecutively by measuring the absorption (i.e., LED on) and emission (i.e., LED off) intensity [47]. For each sequence, 20 images were recorded continuously to improve the signal-to-noise ratio (SNR). Band-pass filters (central wavelength 660 nm) are utilized to spectrally filter the measured signal for both LOSA and LFI measurements. A typical averaged transmissivity image of

Condition 2 is shown in Fig. 12. The SNR of the acquired data was meticulously measured and analyzed. The maximum observed SNR is about 50 dB, which aligns closely with the levels of noise intentionally introduced in the numerical simulations.

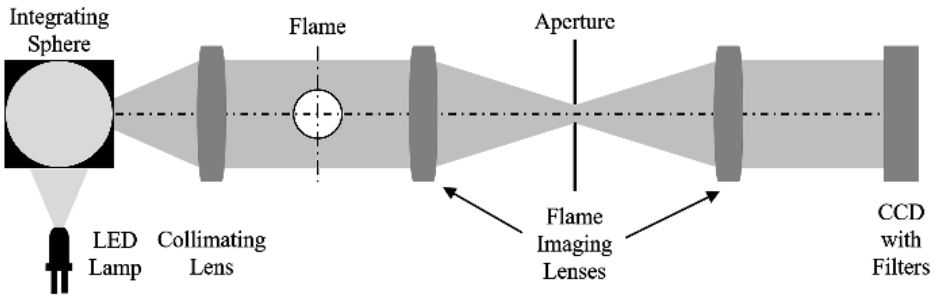

Fig. 11. Optical configuration for absorption coefficient measurements.

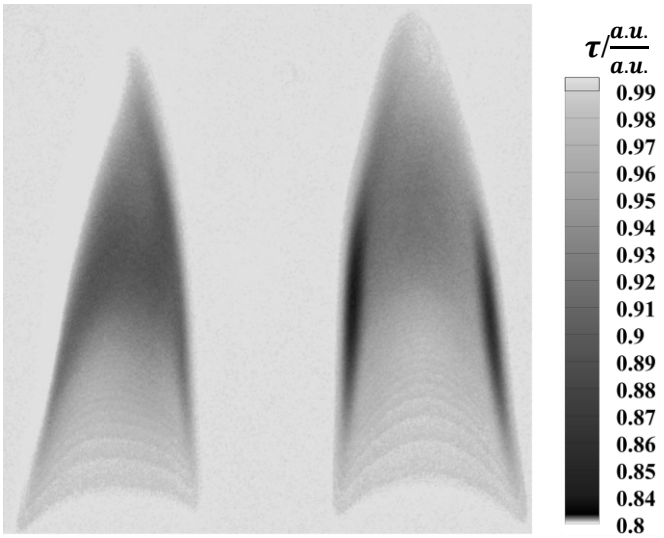

Fig. 12. Example of an average transmissivity image collected by LOSA for Condition 2.

4.1. Reconstruction of bimodal flame absorption coefficient

A comprehensive 3-D coordinate system is established and illustrated in Fig. 9(b). The central point of the burner is defined as the coordinate origin, denoted as (0, 0, 0). Subsequently, the X-axis is carefully oriented parallel to the horizontal alignment of the burner nozzle's centerline, whereas the Y-axis is precisely aligned with the vertical orientation of the burner nozzle's centerline. Concurrently, the Z-axis is effectively oriented to correspond to the direction associated with flame height. Ten directions (0°, 30°, 60°, 120°, 150°, 180°, 210°, 240°, 300° and 330° concerning the Y-axis) without angular occlusion between the flames are selected for the LOSA measurements to obtain transmissivity images. The flame was divided into $N_z \times N_r \times N_\varphi = 15 \times 20 \times 20$ voxels. The absorption coefficient distribution was reconstructed as exhibited in Fig. 13. Furthermore, the radial profiles of the reconstructed soot absorption coefficients at various heights are presented in Fig. 14.

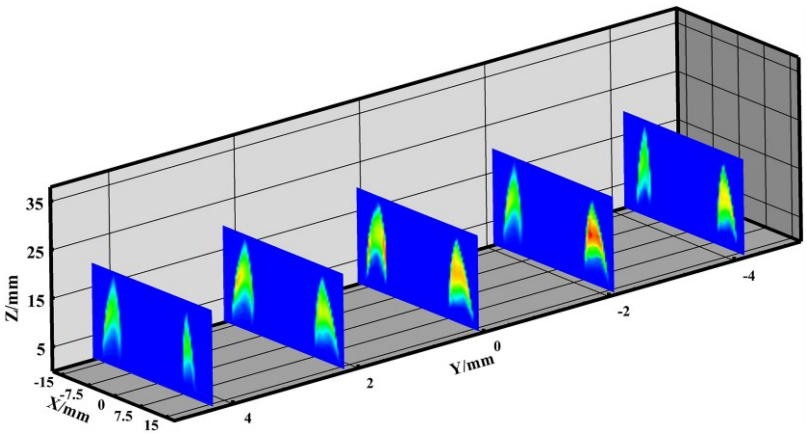

(a) Condition 1

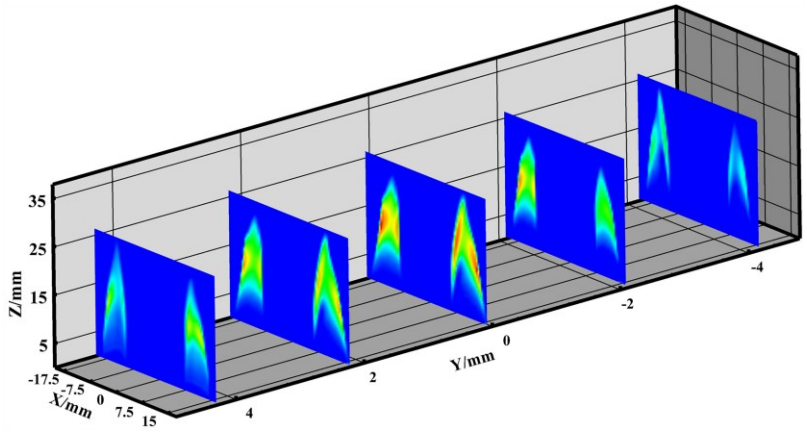

(b) Condition 2

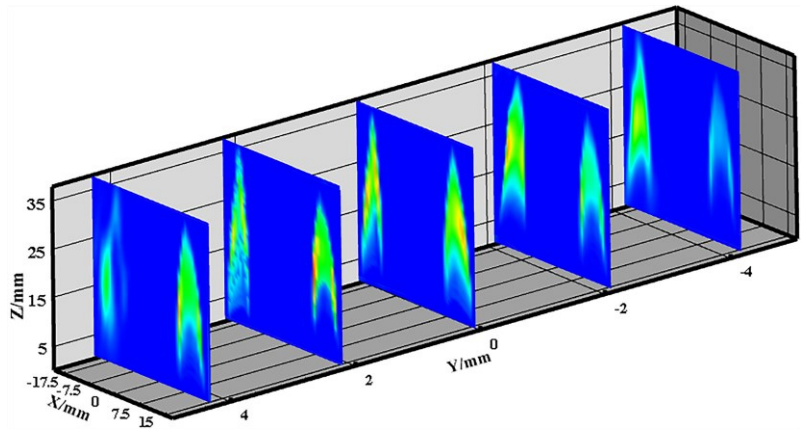

(c) Condition 3

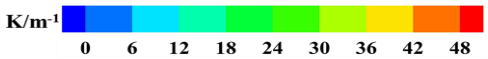

Fig. 13. Reconstructed bimodal flame absorption coefficient distributions.

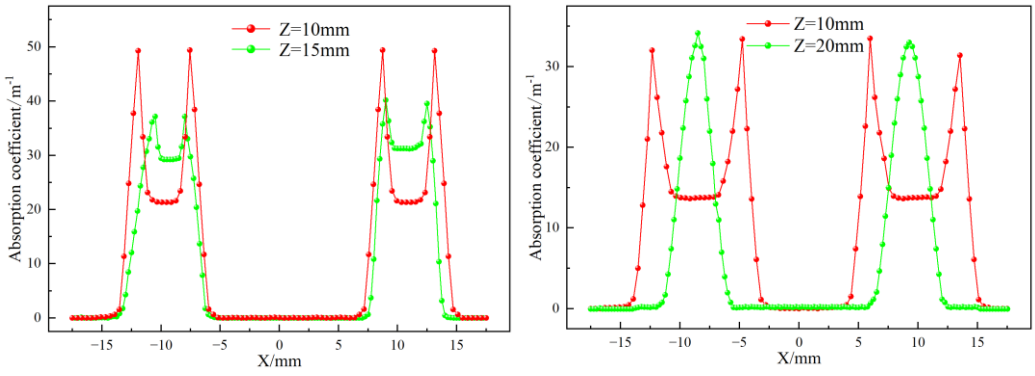

(a) Condition 1 (b) Condition 2

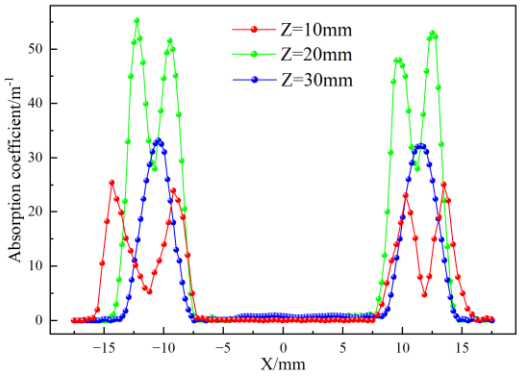

(c) Condition 3

Fig. 14. Radial profiles of reconstructed soot absorption coefficient at different heights.

As evident from both Figs. 13 and 14, when considering one of the flame peaks as a reference, it becomes apparent that there is a lack of adequate interaction between the fuel and oxygen at the central axis of the fuel nozzle, leading to an incomplete combustion reaction that generates low levels of polycyclic aromatic hydrocarbons (PAHs) for soot. As the distance from the central axis increases, the fuel and oxygen interact more efficiently, accelerating the reaction rate and increasing the production of soot until it reaches a peak. Following this peak, the fuel concentration decreases and the rate of soot oxidation becomes dominant, resulting in a rapid decline in the soot until it is eliminated. The axial distribution of the absorption coefficient exhibits the same trend, i.e., an initial increase followed by a decrease as it extends outward from the outlet of the fuel nozzle. The phenomenon of flame tilt towards the burner center is due to a reduction in the concentration of oxygen between the flames and an increase in the axial velocity [48]. The reconstruction time for absorption coefficients under three different conditions is approximately 140s, consistent with the numerical simulations conducted using the same voxel numbers. The maximum absorption coefficients achieved under three operating conditions are 54.82 m^{-1}, 50.18 m^{-1}, and 56.44 m^{-1}, respectively. Notably, these coefficients exhibit a non-monotonic relationship with the increasing fuel concentration. This intricate behaviour can be attributed to the complex interaction between early soot nucleation, surface growth and oxidation mechanisms. Increasing fuel concentration reduces the flame peak temperature, which in turn reduces fuel pyrolysis, suppresses the generation of hydrocarbon radicals and H atoms, and mitigates the formation of soot particles. The reduction of flame peak temperature also decreases the surface growth rate of soot [49]. Moreover, the increased fuel concentration also partially inhibits the oxidation mechanism of soot, thus, mitigating the reaction between flame

radicals (OH, O) and soot and reducing the overall oxidation of soot. However, the present absorption coefficient results show a good agreement with those previously reported to refs. [50, 51] in terms of both profiles and amplitudes.

4.2. Reconstruction of bimodal flame temperature

To improve the SNR, ten images were recorded continuously. The noise of the photosensor was eliminated before reconstruction. The flame was divided into $N_z \times N_r \times N_\varphi$=15×20×20 voxels. The flame temperature distribution was reconstructed and exhibited in Fig. 15. It can be observed that the temperature distributions are within the range of 1000-2100 K and exhibit a distinct pattern. The reconstruction time for temperature under three different conditions is approximately 700s, showing consistency with the numerical simulations as well. The maximum temperatures achieved for Conditions 1, 2 and 3 are 2195 K, 2176 K and 2147 K, respectively. It is evident that as the fuel flow rates increase, the intensity of soot formation also increases. This occurs due to relative oxygen deprivation, which increases the radiative heat loss.

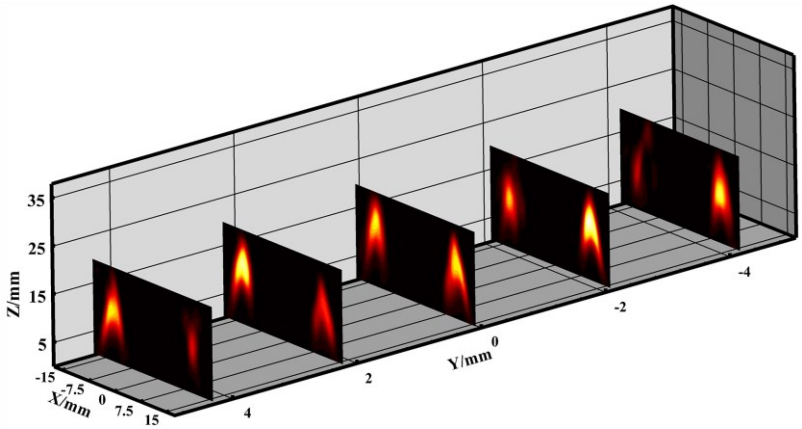

(a) Condition 1

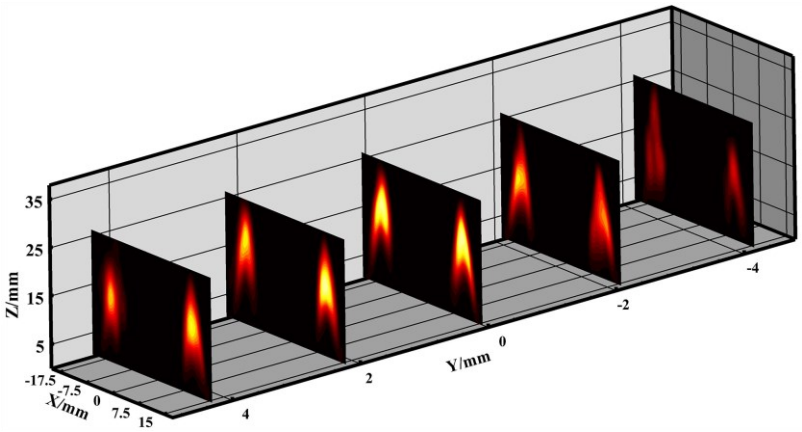

(b) Condition 2

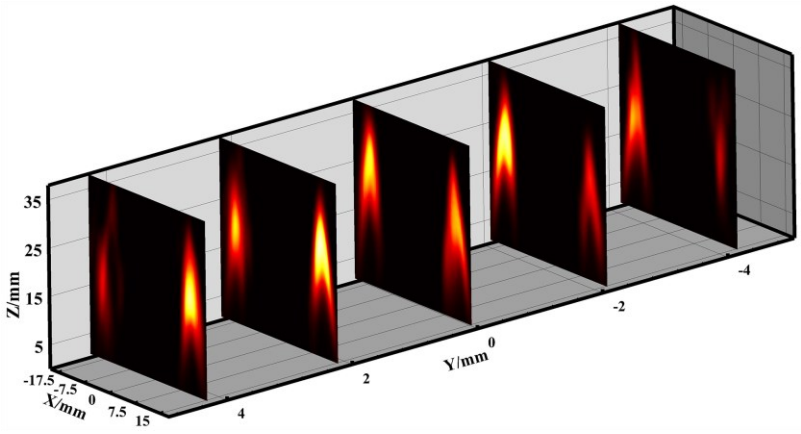

(c) Condition 3

Fig. 15. Reconstructed bimodal flame temperature distributions.

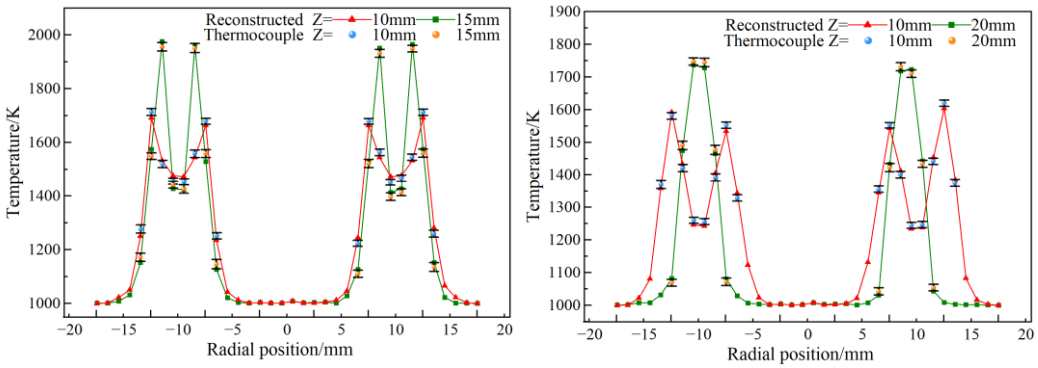

(a) Condition 1 (b) Condition 2

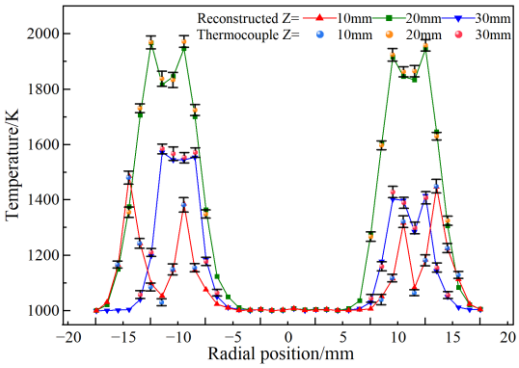

(c) Condition 3

Fig. 16. Comparison of reconstructed temperatures with thermocouple measurements.

To validate the accuracy of the reconstructed flame temperature, an R-type thermocouple was utilized to measure the flame temperature in the radial direction at various heights. The measured results of the flame temperature were corrected to consider the radiation heat loss of the medium to the surroundings and the conduction heat loss of the thermocouple junctions [52]. At each sampling point, fifty consecutive readings were collected. Fig. 16 presents a comparison between the thermocouple measurements and the reconstructed flame temperature, with the standard

deviations for the thermocouple measurements also displayed. There is a high degree of agreement between the thermocouple measurements and the reconstructed results. The maximum difference of 68 K is observed at z = 20 mm (Condition 3).

In order to offer valuable insights into the performance of the reconstruction techniques, especially concerning the handling of discontinuities along the z-axis, the temperature profiles along the centerline of the z-axis (Y=0) under Condition 3 is depicted in Fig. 17. Notably, the temperature is relatively low near the outlet of the fuel nozzle due to the incomplete mixing of fuel and air. However, as the mixture infiltrates the combustion zone, the temperature rises due to the exothermic combustion reaction. Beyond the flame front, the temperature starts to decline as the combustion products (water vapor, carbon dioxide, etc.) mix with the surrounding air and move away from the reaction zone.

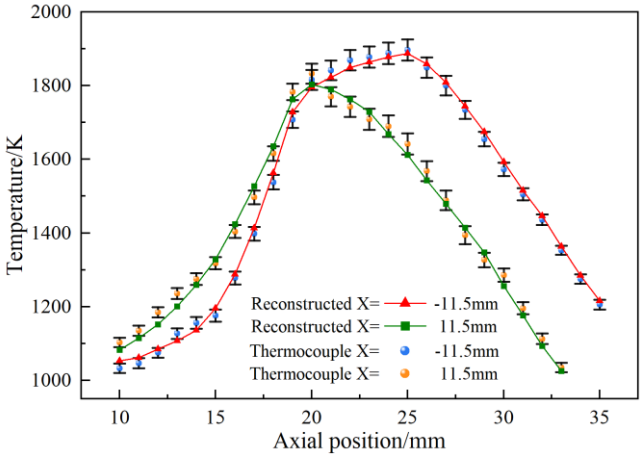

Fig. 17. Reconstructed temperature profiles along the centerline of the z-axis (Y=0) under Condition 3.

4.3. Reconstruction of Gülder burner flame

Further verifications of the proposed method were conducted through the Gülder burner flame, with reference values from Ref. [53] considered in the analysis. Specifically, a similar ethylene flow rate was set i.e., 0.194 L/min. However, due to the limitations of the mass flow controller's range, the air flow rate in this study was set to 30 L/min, whereas in Ref. [53], it was set to 284 L/min. Comparative analyses were extended to other optical methods mentioned for reconstructing the flame temperature. The outcomes of these cases are visually depicted in Fig. 18. The absorption coefficient and temperature reconstruction results of the proposed method are depicted in (b1) and (c1), respectively, while those of Ref. [53] are presented in (b2) and (c2), respectively. Notably, (c3) involved reconstructing the flame temperature using a soot absorption coefficient of 10 m^{-1} [30], while (c4) represented the proposed method without extracting flame-containing voxels and filtering effective rays. The temperature reconstruction results under different reconstruction methods are displayed in Table 5 for a clearer presentation.

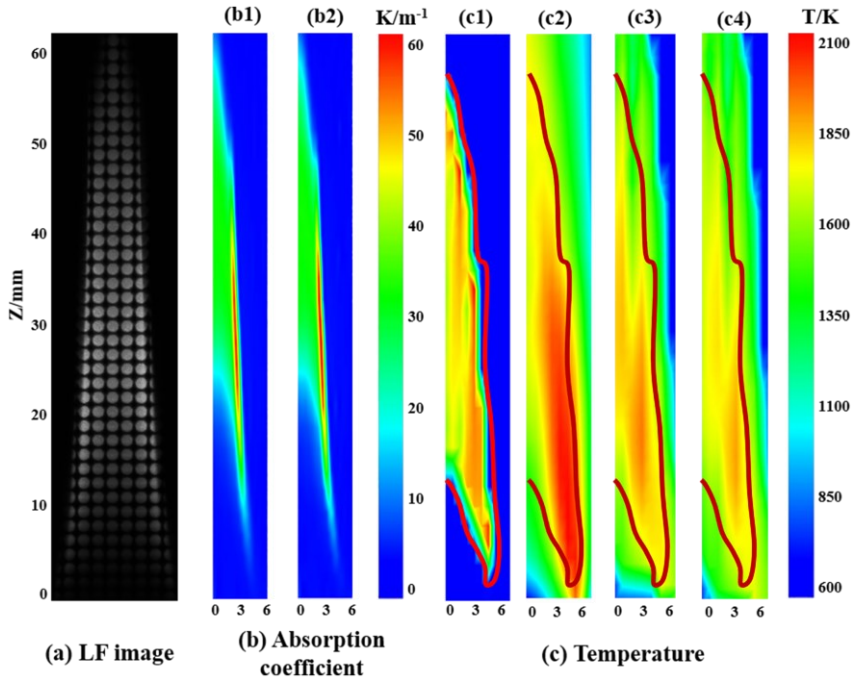

Fig. 18. Comparison results of flame temperature and absorption coefficient. (a) Example of a raw LF flame image, (b) Absorption coefficient (b1: proposed method, b2: Ref. [53]), and (c) Temperature (c1: proposed method, c2: Ref. [53], c3: Ref. [30], c4: without extracting the flame-containing voxels).

Table 5. The temperature reconstruction results under different reconstruction methods.

Case	Peak temperature/K	Peak temperature relative error compared to [53]/%	Overall relative error compared to [53]/%
c1: Proposed method	2118	1.76	7.36
c2: [53]	2156	/	/
c3: [30]	2046	5.10	8.36
c4: without extracting the flame-containing voxels	2027	5.98	10.03

It can be seen that the absorption coefficient distributions exhibit a similar trend with the Ref. [53]. Both distributions show peak absorption coefficients within the flame annulus with values of 58.28 m^{-1} and 59.09 m^{-1}, respectively (i.e., corresponding to the soot volume fraction of 7.91 ppm and 8.02 ppm). When considering the absorption coefficient distribution across the entire domain, the overall relative error of 1.32% is achieved through the proposed method. This indicates that the method proposed provides precise results concerning both the range and distribution region of the absorption coefficient.

Fig. 18(c) displays the reconstructed temperature distributions and in all cases, peak temperatures are located in the wing of the flames. The reference value of the peak temperature is 2156 K, and the reference distribution of the temperature is shown in Fig. 18(c2) [53]. The peak temperature and relative errors for all cases are presented in Table 5. Notably, the proposed method yields a peak temperature of 2118 K. Meanwhile, peak temperatures recorded in

(c3) and (c4) are 2046 K and 2027 K, respectively. Relative errors for peak temperatures across these methods are 1.76%, 5.10%, and 5.98%, respectively. Considering the reference temperature distribution, overall relative errors are 7.36%, 8.36%, and 10.03%, respectively. It's worth noting that for all cases, including c2, c3, and c4, the error is calculated using the reference boundaries as outlined in c1. These findings affirm the effectiveness and accuracy of the proposed method.

5. Conclusions

This study presents a novel approach for retrieving the 3-D soot absorption coefficient and temperature of flames by combining the line-of-sight attenuation and light field imaging techniques. The effectiveness of the proposed method was verified through numerical simulations. These simulations involved a comprehensive exploration of diverse factors, including noise levels, a comparative study with recent light field reconstruction techniques, and the manipulation of flame-dividing voxel numbers. Experimental studies were also carried out to further validate the applicability of the proposed method. The conclusions derived from this study are summarized below:

- Compared to the currently adopted light field imaging-based reconstruction methods, the proposed method demonstrates a higher accuracy in reconstructing the 3-D flame temperature and providing shorter reconstruction times.
- The proposed method also demonstrates an effective noise resistance for an accurate reconstruction of soot absorption coefficient and temperature distributions. Even in the presence of a 5% noise level, the mean absorption coefficient and temperature reconstruction relative error remain remarkably low at 1.64% and 1.01%, respectively.
- The experimental results of bimodal flame temperature reconstruction exhibit an excellent agreement with thermocouple measurement with a maximum difference of 68 K. For axisymmetric diffusion flames, the reconstructed absorption coefficients and temperature also demonstrate a good agreement with the literature.

Future works will be focused on developing an optical system for the transient measurement of 3-D soot absorption coefficients and temperature in unsteady flames.

Declaration of Competing Interest

The authors declare that they have no known competing financial interests or personal relationships that could have appeared to influence the work reported in this paper.

CRediT authorship contribution statement

Tianxiang Ling: Conceptualization, Methodology, Software, Writing – original draft. **Guoqing Chen:** Conceptualization, Formal analysis, Investigation. **Md. Moinul Hossain:** Writing – review & editing. **Qi Qi:** Data curtion, Validation. **Biao Zhang:** Software, Resources. **Chuanlong Xu:** Supervision, Writing – review & editing.

Data availability

The data that support the findings of this study are available from the corresponding authors upon reasonable

request.

Acknowledgments

The authors wish to express their gratitude to the National Natural Science Foundation of China (Nos. 52376158, 52176167) and the Fundamental Research Funds for the Central Universities (No. 2242023K30058) for supporting this research.

References

[1] M.R. Kholghy, Y. Afarin, A.D. Sediako, J. Barba, M. Lapuerta, C. Chu, J. Weingarten, B. Borshanpour, V. Chernov, M.J. Thomson, Comparison of multiple diagnostic techniques to study soot formation and morphology in a diffusion flame, Combustion and Flame, 176 (2017) 567-583.

[2] R.J. Huang, Y. Zhang, C. Bozzetti, K.F. Ho, J.J. Cao, Y. Han, K.R. Daellenbach, J.G. Slowik, S.M. Platt, F. Canonaco, P. Zotter, R. Wolf, S.M. Pieber, E.A. Bruns, M. Crippa, G. Ciarelli, A. Piazzalunga, M. Schwikowski, G. Abbaszade, J. Schnelle-Kreis, R. Zimmermann, Z. An, S. Szidat, U. Baltensperger, I. El Haddad, A.S. Prevot, High secondary aerosol contribution to particulate pollution during haze events in China, Nature, 514 (2014) 218-222.

[3] Y. Wang, S.H. Chung, Soot formation in laminar counterflow flames, Prog Energy Combust Sci, 74 (2019) 152-238.

[4] R. Viskanta, M.P. Menguc, Radiation heat transfer in combustion systems, Prog Energy Combust Sci, 13 (1987) 97-160.

[5] R.S. Barlow, Laser diagnostics and their interplay with computations to understand turbulent combustion, Proc Combust Inst, 31 (2007) 49-75.

[6] Q.N. Chan, P.R. Medwell, P.A.M. Kalt, Z.T. Alwahabi, B.B. Dally, G.J. Nathan, Simultaneous imaging of temperature and soot volume fraction, Proc Combust Inst, 33 (2011) 791-798.

[7] C. Lou, C. Chen, Y. Sun, H. Zhou, Review of soot measurement in hydrocarbon-air flames, Science China Technological Sciences, 53 (2010) 2129-2141.

[8] H. Liu, S. Zheng, H. Zhou, Measurement of Soot Temperature and Volume Fraction of Axisymmetric Ethylene Laminar Flames Using Hyperspectral Tomography, IEEE Transactions on Instrumentation and Measurement, 66 (2017) 315-324.

[9] W. Yan, C. Lou, Two-dimensional distributions of temperature and soot volume fraction inversed from visible flame images, Experimental Thermal and Fluid Science, 50 (2013) 229-233.

[10] D.R. Snelling, K.A. Thomson, G.J. Smallwood, O.L. Guider, E.J. Weckman, R.A. Fraser, Spectrally Resolved Measurement of Flame Radiation to Determine Soot Temperature and Concentration, AIAA Journal, 40 (2002) 1789-1795.

[11] Q. Huang, F. Wang, J. Yan, Y. Chi, Simultaneous estimation of the 3-D soot temperature and volume fraction distributions in asymmetric flames using high-speed stereoscopic images, Appl Opt, 51 (2012) 2968-2978.

[12] M.M. Hossain, G. Lu, D. Sun, Y. Yan, Three-dimensional reconstruction of flame temperature and emissivity distribution using optical tomographic and two-colour pyrometric techniques, Meas Sci Technol, 24 (2013) 074010.

[13] M. Ni, H. Zhang, F. Wang, Z. Xie, Q. Huang, J. Yan, K. Cen, Study on the detection of three-dimensional soot temperature and volume fraction fields of a laminar flame by multispectral imaging system, Applied Thermal Engineering, 96 (2016) 421-431.

[14] H. Chen, P.M. Lillo, V. Sick, Three-dimensional spray–flow interaction in a spark-ignition direct-injection engine, Int J Engine Res, 17 (2015) 129-138.
[15] H. Chen, V. Sick, Three-Dimensional Three-Component Air Flow Visualization in a Steady-State Engine Flow Bench Using a Plenoptic Camera, SAE Int J Engines, 10 (2017) 625-635.
[16] N. Zeller, F. Quint, U. Stilla, Depth estimation and camera calibration of a focused plenoptic camera for visual odometry, ISPRS-J Photogramm Remote Sens, 118 (2016) 83-100.
[17] J. Sun, C. Xu, B. Zhang, M.M. Hossain, S. Wang, H. Qi, H. Tan, Three-dimensional temperature field measurement of flame using a single light field camera, Opt Express, 24 (2016) 1118-1132.
[18] S. Wen, H. Qi, S.-B. Liu, Y.-T. Ren, J.-W. Shi, X. Huang, A hybrid LSQP algorithm for simultaneous reconstruction of the temperature and absorption coefficient field from the light-field image, Infrared Phys Technol, 105 (2020) 103196.
[19] J. Li, M.M. Hossain, J. Sun, Y. Liu, B. Zhang, C. Tachtatzis, C. Xu, Simultaneous measurement of flame temperature and absorption coefficient through LMBC-NNLS and plenoptic imaging techniques, Applied Thermal Engineering, 154 (2019) 711-725.
[20] X. Huang, H. Qi, C. Niu, L. Ruan, H. Tan, J. Sun, C. Xu, Simultaneous reconstruction of 3D temperature distribution and radiative properties of participating media based on the multi-spectral light-field imaging technique, Applied Thermal Engineering, 115 (2017) 1337-1347.
[21] C.-Y. Niu, H. Qi, X. Huang, L.-M. Ruan, H.-P. Tan, Efficient and robust method for simultaneous reconstruction of the temperature distribution and radiative properties in absorbing, emitting, and scattering media, Journal of Quantitative Spectroscopy and Radiative Transfer, 184 (2016) 44-57.
[22] C.-Y. Niu, H. Qi, X. Huang, L.-M. Ruan, W. Wang, H.-P. Tan, Simultaneous reconstruction of temperature distribution and radiative properties in participating media using a hybrid LSQR–PSO algorithm, Chin Phys B, 24 (2015) 114401.
[23] Q. Qi, M.M. Hossain, J.J. Li, B. Zhang, J. Li, C.L. Xu, Approach to reduce light field sampling redundancy for flame temperature reconstruction, Opt Express, 29 (2021) 13094-13114.
[24] Q. Qi, M.M. Hossain, B. Zhang, T. Ling, C. Xu, Flame temperature reconstruction through a multi-plenoptic camera technique, Meas Sci Technol, 30 (2019) 124002.
[25] H.A. Michelsen, Probing soot formation, chemical and physical evolution, and oxidation: A review of in situ diagnostic techniques and needs, Proceedings of the Combustion Institute, 36 (2017) 717-735.
[26] M. Kholghy, M. Saffaripour, C. Yip, M.J. Thomson, The evolution of soot morphology in a laminar coflow diffusion flame of a surrogate for Jet A-1, Combust Flame, 160 (2013) 2119-2130.
[27] F. Migliorini, K.A. Thomson, G.J. Smallwood, Investigation of optical properties of aging soot, Appl Phys B, 104 (2011) 273-283.
[28] M.R. Kholghy, A. Veshkini, M.J. Thomson, The core-shell internal nanostructure of soot - A criterion to model soot maturity, Carbon, 100 (2016) 508-536.
[29] A. D'Anna, A. Rolando, C. Allouis, P. Minutolo, A. D'Alessio, Nano-organic carbon and soot particle measurements in a laminar ethylene diffusion flame, Proc Combust Inst, 30 (2005) 1449-1456.
[30] Y. Yuan, T.-J. Li, Y.-L. Zhu, Y. Shuai, H.-P. Tan, Influence analysis of radiative properties and flame temperature reconstruction based on optical tomography, Int J Heat Mass Transfer, 126 (2018) 342-352.
[31] T.-J. Li, C.-X. Zhang, Y. Yuan, Y. Shuai, H.-P. Tan, Effect of nonuniform radiation properties on flame temperature reconstruction based on light field imaging, Int Commun Heat Mass Transfer, 104 (2019) 136-146.
[32] J. Yon, J. Jose Cruz, F. Escudero, J. Moran, F. Liu, A. Fuentes, Revealing soot maturity based on multi-

wavelength absorption/emission measurements in laminar axisymmetric coflow ethylene diffusion flames, Combust Flame, 227 (2021) 147-161.
[33] G. Legros, Q. Wang, J. Bonnety, M. Kashif, C. Morin, J.-L. Consalvi, F. Liu, Simultaneous soot temperature and volume fraction measurements in axis-symmetric flames by a two-dimensional modulated absorption/emission technique, Combustion and Flame, 162 (2015) 2705-2719.
[34] T.P. Jenkins, R.K. Hanson, Soot pyrometry using modulated absorption/emission, Combust Flame, 126 (2001) 1669-1679.
[35] M. Levoy, Z. Zhang, I. McDowall, Recording and controlling the 4D light field in a microscope using microlens arrays, J Microsc, 235 (2009) 144-162.
[36] J. Sun, M.M. Hossain, C.-L. Xu, B. Zhang, S.-M. Wang, A novel calibration method of focused light field camera for 3-D reconstruction of flame temperature, Opt Commun, 390 (2017) 7-15.
[37] Q. Qi, C. Xu, M.M. Hossain, J. Li, B. Zhang, J. Li, Simultaneous reconstruction of flame temperature and soot volume fraction through weighted non-negative least squares and light field imaging techniques, Fuel, 336 (2023).
[38] J.D. Felske, C.L. Tien, Calculation of the Emissivity of Luminous Flames, Combust Sci Technol, 7 (2007) 25-31.
[39] R.J. Hall, P.A. Bonczyk, Sooting flame thermometry using emission/absorption tomography, Appl Opt, 29 (1990) 4590-4598.
[40] U.O. Koylu, G.M. Faeth, Structure of overfire soot in buoyant turbulent diffusion flames at long residence times, Combust Flame, 89 (1992) 140-156.
[41] R. Bro, S. DeJong, A fast non-negativity-constrained least squares algorithm, J Chemom, 11 (1997) 393-401.
[42] R.J. Santoro, T.T. Yeh, J.J. Horvath, H.G. Semerjian, The Transport and Growth of Soot Particles in Laminar Diffusion Flames, Combust Sci Technol, 53 (1987) 89-115.
[43] Y. Liu, M. Zhu, T. Wang, G. Lei, M.M. Hossain, B. Zhang, J. Li, C. Xu, Spatial resolution of light field sectioning pyrometry for flame temperature measurement, Opt Lasers Eng, 140 (2021) 106545.
[44] M.D. Smooke, M.B. Long, B.C. Connelly, M.B. Colket, R.J. Hall, Soot formation in laminar diffusion flames, Combust Flame, 143 (2005) 613-628.
[45] D.R. Snelling, K.A. Thomson, G.J. Smallwood, O.L. Gulder, Two-dimensional imaging of soot volume fraction in laminar diffusion flames, Appl Opt, 38 (1999) 2478-2485.
[46] P.S. Greenberg, J.C. Ku, Soot volume fraction imaging, Appl Opt, 36 (1997) 5514-5522.
[47] F. Escudero, A. Fuentes, R. Demarco, J.L. Consalvi, F. Liu, J.C. Elicer-Cortés, C. Fernandez-Pello, Effects of oxygen index on soot production and temperature in an ethylene inverse diffusion flame, Experimental Thermal and Fluid Science, 73 (2016) 101-108.
[48] T. Hirasawa, K. Gotanda, H. Masuda, Y. Nakamura, Impact of Flame–Flame Interactions in Identical Twin Diffusion Microflames, Combust Sci Technol, 184 (2012) 1651-1663.
[49] K.O. Lee, C.M. Megaridis, S. Zelepouga, A.V. Saveliev, L.A. Kennedy, O. Charon, F. Ammouri, Soot formation effects of oxygen concentration in the oxidizer stream of laminar coannular nonpremixed methane/air flames, Combust Flame, 121 (2000) 323-333.
[50] M. Kashif, J. Bonnety, P. Guibert, C. Morin, G. Legros, Soot volume fraction fields in unsteady axis-symmetric flames by continuous laser extinction technique, Opt Express, 20 (2012) 28742-28751.
[51] C.P. Arana, M. Pontoni, S. Sen, I.K. Puri, Field measurements of soot volume fractions in laminar partially premixed coflow ethylene/air flames, Combustion and Flame, 138 (2004) 362-372.
[52] C.S. McEnally, U.O. Koylu, L.D. Pfefferle, D.E. Rosner, Soot volume fraction and temperature measurements in laminar nonpremixed flames using thermocouples, Combust Flame, 109 (1997) 701-720.

[53] F.S. Liu, H.S. Guo, G.J. Smallwood, O.L. Gulder, Effects of gas and soot radiation on soot formation in a coflow laminar ethylene diffusion flame, J Quant Spectrosc Radiat Transfer, 73 (2002) 409-421.